

Hierarchical Random Walker Segmentation for Large Volumetric Biomedical Images

Dominik Drees, Florian Eilers and Xiaoyi Jiang *Senior Member, IEEE*

Abstract—The random walker method for image segmentation is a popular tool for semi-automatic image segmentation, especially in the biomedical field. However, its linear asymptotic run time and memory requirements make application to 3D datasets of increasing sizes impractical. We propose a hierarchical framework that, to the best of our knowledge, is the first attempt to overcome these restrictions for the random walker algorithm and achieves sublinear run time and constant memory complexity. The goal of this framework is – rather than improving the segmentation quality compared to the baseline method – to make interactive segmentation on out-of-core datasets possible. The method is evaluated quantitatively on synthetic data and the CT-ORG dataset where the expected improvements in algorithm run time while maintaining high segmentation quality are confirmed. The incremental (i.e., interaction update) run time is demonstrated to be in seconds on a standard PC even for volumes of hundreds of Gigabytes in size. In a small case study the applicability to large real world from current biomedical research is demonstrated. An implementation of the presented method is publicly available in version 5.2 of the widely used volume rendering and processing software Voreen¹.

Index Terms—Volume Segmentation, Hierarchical Processing, Random Walk

I. INTRODUCTION

While the study of structures in 3D datasets is important in many contexts, especially in the biomedical field [1], [2], [3], visual inspection based analysis is error-prone [4]. For quantifiable results or novel insights into properties of the data invisible to the human observer, automatic techniques are required. For many analysis techniques (from simple volume/area comparisons to complex structure analysis [5]) binary segmentation is an important intermediate step. At the same time, improvements in imaging technologies (for example in light sheet microscopy) are providing images of increasing resolution and size (with hundreds of Gigabytes or even Terabytes for a single dataset). While this opens the door for biomedical research [6], [7], it also poses problems for image analysis algorithms that need to be solved to further advance biomedical and other research with new technology providing quantifiable results.

The random walker method for image segmentation [8], [9] is a popular technique for interactively creating arbitrary segmentations of 3D (or 2D) datasets. From user-defined initial

seeds for semantically different regions of the image, the complete image is labeled based on local connectivity and voxel-wise similarity. A problem for the application of this technique on larger datasets is its lacking scalability: For a dataset with n voxels, it requires $\Theta(n)$ memory (with a high constant factor) and $\Omega(n)$ computation time even for a very local update of the set of seeds. In practice, even for datasets smaller than 100 MB, minutes of computation time and large portions of the available graphics or main memory of a standard PC are required, a problem that is not fundamentally solved by earlier extensions to the method [9].

Contributions: We present a hierarchical, level-of-detail (LOD) pyramid-based framework that, to the best of our knowledge for the first time, allows random walker image segmentation to be applied to out-of-core (i.e., larger than main memory) datasets. The core idea of hierarchical refinement of an initial coarse application of the basic method in constant sized bricks achieves constant memory requirements while further optimizations such as pruning result in an observed sublinear run time. Using our technique, incremental updates can often be computed in seconds even for 100 GB and larger volumes on commodity hardware. The goal of this paper is explicitly *not* the improvement of segmentation quality. However, we show that segmentation quality is comparable to the baseline method with our framework. While this work focuses on binary image segmentation and the 3D case, a generalization to multi-class labeling and to 2D data is conceivable.

We believe that the presented method is useful, for example, to apply existing RW-based pipelines [10], [11], [12] to large datasets, or as a highly efficient labeling tool for machine learning applications.

The remainder of the paper is organized as follows. After presenting related work and two fundamental concepts, the proposed framework will be described in detail. Subsequently, an evaluation on synthetic data, the CT-ORG dataset and real data from current biomedical research is presented and discussed, followed by the conclusion.

II. RELATED WORK

The seminal work of Grady [8] is the basis of a large number of publications with applications in biomedicine (fluorescent cell tracking [13], pap smear cells [14], tumor [15], [16], placenta [12], airway segmentation [10], [17], multimodal problems [18], [19] and geophysical research [20]). It is also used in other algorithms (image superpixel segmentation [21], [22] and deep learning techniques [23]).

D. Drees, F. Eilers and X. Jiang are with the Faculty of Mathematics and Computer Science, University of Münster, Münster, Germany.

F. Eilers is a member of CiM-IMPRS, the joint graduate school of the Cells-in-Motion Interfaculty Centre, University of Münster, Germany and the International Max Planck Research School - Molecular Biomedicine, Münster, Germany.

¹<https://www.uni-muenster.de/Voreen/>

Research to extend the basic idea is still ongoing, for example on automatic seed generation [24]. Yang et al. augmented the method for interactive boundary definition [25]. The automatic choice of edge weighting functions has been tackled using statistical models [26] and an end-to-end learning [27]. Li et al. [28] improve the convergence of the random walker method and reduce the seed sensitivity using a continuous random walk model with coherence regularization for the extracted foreground region. Prassni et al. [29] proposed uncertainty visualization guiding label placement in interactive 3D volume segmentation. However, resource requirements of the random walker method hinder application in some cases. Xiao and Hu [30] apply Grady’s method in a two-step (“hierarchical”) procedure to first identify an abnormal region and then a tumor within. They note that during the evaluation “12 groups failed due to high space complexity of RW”.

Ge et al. [31] propose a hierarchical strategy for the related graph-cut method [32]. The authors suggest creating an initial segmentation on the coarsest level of a LOD-pyramid and using finer levels for refinement of segmentation boundaries. Their method, however, neither reduces the memory requirements, nor results in sublinear run time, as the propagation of intermediate segmentation results to the next layer still operates on the whole image.

Fabijanska and Goclawski [33] apply the random walker method on superpixels. While reducing the size of the linear equation system by roughly 90%, the pre-processing step still requires random access to the full image and introduces two parameters, changes to which require a complete recomputation, hindering interactive use on large datasets.

Biomedisa [34] is a recent platform for biomedical image segmentation that performs interpolation of sparsely pre-segmented slices based on simulation of random walker agents. Despite testing on a powerful system (750 GB RAM and 4 NVIDIA Tesla V100) the authors had to split a moderately sized dataset of $900 \times 1303 \times 4327$ voxels for processing.

To the best of our knowledge there is no prior work on frameworks that allow the random walker method to be applied to images that exceed the main or graphics memory.

Finally, artificial neural network approaches have become increasingly popular [35], [36] which, depending on the problem, network design and receptive field, may also be suitable for large volume segmentation. Nevertheless, random walker based methods remain popular [37]. This may be due to the fact that high level of complexity (large amount of ground truth (GT) data, hyperparameters, etc.) of deep learning based methods hinders fast problem-solving for novel scenarios and diverse image data. Non-learning-based methods like random walker are useful in situations where machine learning is not suitable (few datasets or “ad hoc” segmentation of varying structures of interest), where (at least presently) lacking generalizability hinders application, or where interactive correction of automatic results is required [38]. In other situations, where machine learning is suitable, our work serves as a highly efficient and effective labeling tool. We will further discuss this issue later.

III. FUNDAMENTAL CONCEPTS

This section introduces two known, but vital components of the proposed framework: The octree data structure and the original random walker method.

A. Octree Data Structure

The problem of high performance rendering of large volumetric datasets is, at least partially, solved in visualization, often using an octree data structure (originally introduced by LaMar [39] and Weiler [40] and improved in recent years [41], [42], [43]). Volumes are stored on disk as a brick-based LOD-pyramid from which parts can efficiently be loaded into memory for ray casting.

Similarly, the base structure for the LOD-pyramid in this paper is an octree, recursively defined with nodes $n \in N = N^8 \cup \{\epsilon\}$. A node is either an octuple of child nodes ($n = (c_0, \dots, c_7)$) or empty ($n = \epsilon$). Voxels at any level of the pyramid are stored in *bricks* of s^3 voxels ($b \in B := \mathbb{R}^{s^3}$) with side length s . Each node has an associated brick (via $\text{br}: N \rightarrow B$). $\mathcal{P}(n)$ denotes the parent node of n :

$$\mathcal{P}(n) = \begin{cases} (c_0, \dots, c_7) & \exists i (0 \leq i \leq 7) : c_i = n \\ \epsilon & \text{else} \end{cases}$$

When converting a voxel-grid volume of dimensions $d_x \times d_y \times d_z$ into an octree representation, voxels are chunked into $\frac{d_x}{s} \times \frac{d_y}{s} \times \frac{d_z}{s}$ bricks, each forming a leaf in the octree. The tree is then constructed bottom-up by bundling 2^3 neighboring nodes of one level as children of a new parent node in the next, coarser level until only a single root node remains. The parent node’s associated brick is generated by applying a 2^3 mean filter and downsampling the combined bricks of its children. Here we assume $d_x = d_y = d_z = 2^i \cdot s$, but other volume dimensions can be handled by dynamic transformation and handling of the volume border in the brick-local space. This data structure is illustrated in Figure 1 and described in more detail by Brix et al. [41]. The construction of the octree representation from a single-resolution dataset can be done in linear time and with sub-linear memory requirements, but is not considered in the following, since this is typically done as a one-time preprocessing step that is also required for rendering, or not required at all in cases where instruments already output multi-resolution files.

B. Random Walker Volume Segmentation

The random walker image segmentation method [8] can be used to interactively generate arbitrary foreground/background segmentations in 3D (or 2D) images. The volume (or brick) is viewed as a 3D grid of vertices with edges between 6-neighbors. Vertices $p \in \{1, \dots, s\}^3$ have associated weights defined by the intensity $x(p) = b[p]$, where brackets $b[p]$ denote sampling the intensity from a brick or volume b at position p . Edge weights $w_{p,q}$ are based on the similarity of the connected voxel vertices. Grady suggests $w_{p,q} = \exp(-\beta(b[p] - b[q])^2)$ with β as a free parameter. When interpreting the image graph as an electrical circuit, edges are resistors with weights defining the conductance between

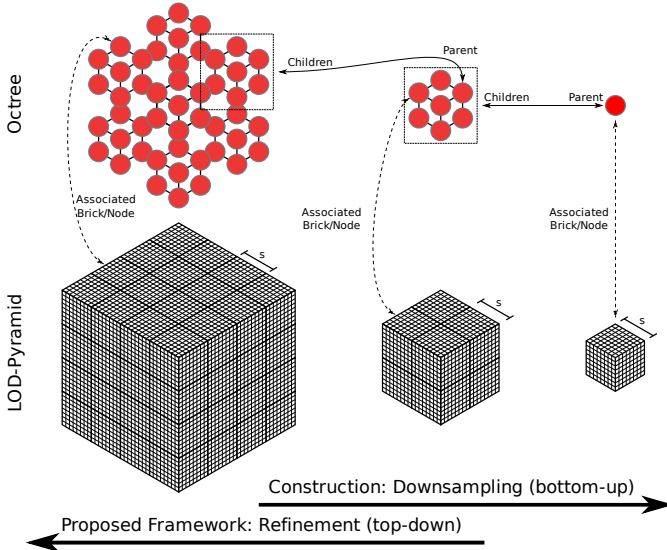


Fig. 1. LOD-Pyramid with Octree used for hierarchical processing. The full resolution dataset (bottom left) is divided into bricks of s^3 voxels, each brick with an associated node. 2^3 nodes with neighboring bricks share a parent node. The parent node's brick is computed by downsampling its children's bricks. The root node's brick is a low resolution version of the input dataset. After the bottom-up construction of the octree, our method uses it in a top-down process.

vertices. Labeled vertices $p_m \in V_m$ are voltage sources with a constant voltage of $x(p) \in \{0, 1\}$, which is set to 0 for background labels and 1 for foreground labels. The weight of an unlabeled vertex $p_u \in V_u$, $x(p_u)$, is the resulting voltage and foreground probability. It can be computed by solving the discrete Dirichlet problem, i.e., by minimizing the Dirichlet integral $D(x) = \frac{1}{2}x^T \mathcal{L}x = \frac{1}{2} \sum_{||p-q||=1} w_{p,q}(x(p) - x(q))^2$ with the boundary condition of predetermined $x(p_m)$ and the Laplacian matrix \mathcal{L} of the image graph. A global minimum can be found by partitioning and reordering x according to V_u and V_m into x_u and x_m and solving $\frac{dD(x_u)}{dx_u} = 0$. While the minimization can be done analytically, it is often faster to use iterative approaches that additionally exploit the sparsity of \mathcal{L} [44]. The experiments in this paper use the conjugate gradient method for this purpose.

IV. HIERARCHICAL FRAMEWORK: METHODS

This section first describes the core concept of our framework that has constant memory requirements, as well as two important extensions of the core idea. Then, a number of further considerations that greatly improve the run time as well as a partial update scheme for interactive segmentation are introduced.

A. Core Concept

The proposed method processes an input octree top-down and at the same time creates the output octree. In each layer, the random walker method for (3D) image segmentation [8] (or a suitable extension [9]) is used to process a brick of the input layer, thus creating a foreground probability map, one brick at a time. Labels are given as structures such as points or curves.

Here, we define individual labels $p \in P = \mathbb{R}^3 \times [0, 1]$ as 3D points with an associated seed value and label sets $l \in L = 2^P$ as groups of labels.

For processing individual bricks, user-defined labels are transformed from volume space into local brick space using a transformation function $\mathcal{T}_n: L \rightarrow L$ (comprising translation and scaling) defined for each node n . After the transformation, labels are rasterized to obtain brick-level seeds to be used in the random walker algorithm.

Let $\text{rw}: B \times L \times \mathbb{R} \rightarrow B$ be the application of the random walker algorithm to a given input brick using a set of labels (in brick-local coordinates) and parameter β . Then, in the first, topmost layer of the LOD-pyramid, i.e., for the root node, the proposed procedure ($\mathcal{H}: N \times L \times \mathbb{R} \rightarrow N$) does not differ much from the basic random walker approach:

$$\text{br}(\mathcal{H}(n, l, \beta)) = \text{rw}(\text{br}(n), \mathcal{T}_n(l), \beta) \quad (1)$$

The output is only defined by the input volume, user labels and β . For subsequent layers, however, the solution for the coarser layer serves as an approximation of the *true* probability map at the current level (if hypothetically computed on the full volume at the current LOD level) and is used to add additional *continuous labels* (with values in the range $[0, 1]$, but not necessarily either 0 or 1) at the border of the current brick, i.e., by upsampling from the coarser level probability map. This way, *global context* (either directly from the parent layer, or transitively via one of its parents) is introduced into the *local foreground probability map*. An example of how a labeled object influences the probabilities in a neighboring brick is illustrated in Figure 2.

The algorithm finishes after processing all leaf level bricks, where the resulting probability bricks define the foreground probability map of the voxel-grid volume that was used to create the input octree.

The hierarchical, local application of the basic method makes the presented approach applicable to arbitrarily large out-of-core datasets. Specifically, since individual bricks and resulting edge weight matrices are comparatively small (depending on s), they can be stored in main or graphics memory. At the same time all computations are local to a single brick or its direct neighborhood, thus require few, linear disk accesses and can be GPU-accelerated. For experiments in this paper the brick size was set to $s = 32$. Larger brick sizes increase the memory requirement (as at least one brick at a time and the resulting linear equation system must be held in memory) and benefit less from pruning/incremental computation (see below). Much smaller bricks cause inaccurate results and disk reads to take a disproportionately large amount of time.

B. Neighborhood Expansion

A remaining question is where the continuous seeds from coarser octree levels should be located. Placing them directly on the border of the current brick means that (since any non-root brick shares 3 of its 6 border faces with its parent, possibly even transitively) in the worst case global context is only established in the root node, so with low resolution. This would result in ragged edges in the resulting probability

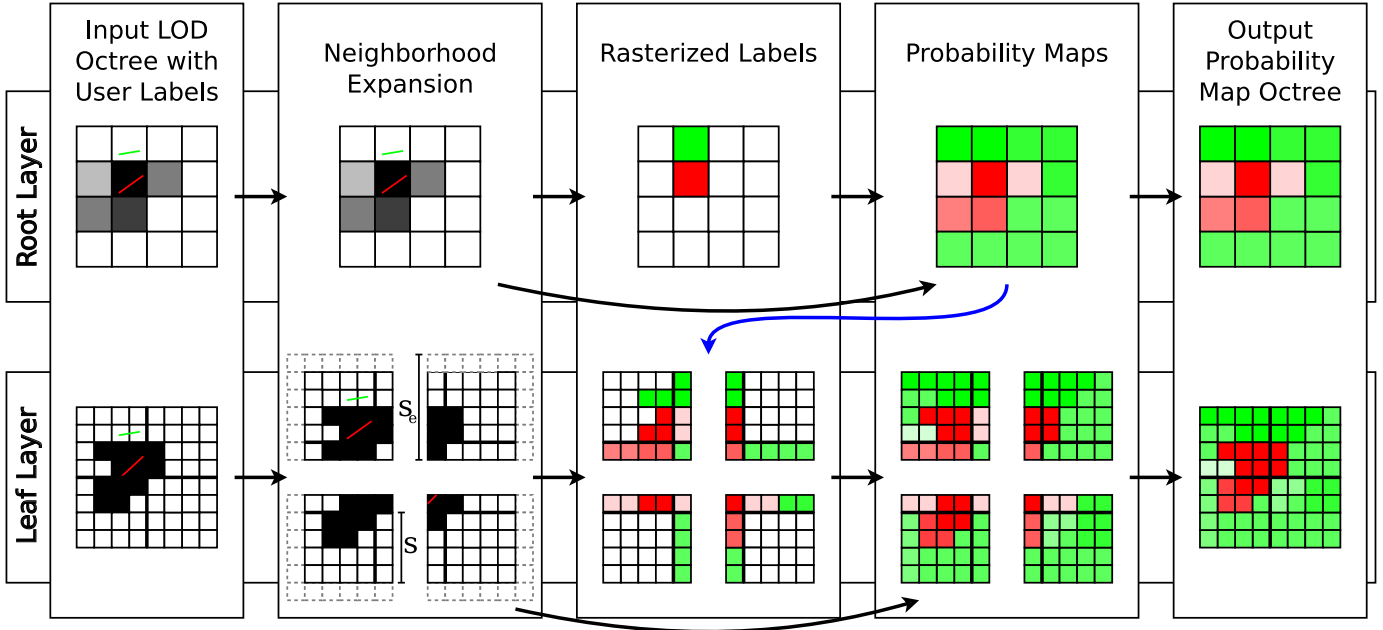


Fig. 2. Exemplary (2D) illustration of the proposed method: The input volume octree is processed top-down, rasterizing user labels for each brick and introducing global context into the local computation by initializing border seeds from solutions of a coarser level (blue arrow). These labels and the input volume brick are used as input for the random walker method which creates the output probability map for the current brick. In a more complex case, intermediate layers would be included in the top-down process, using the probability map of the previous layer and providing global context for the next layer via its probability map.

map. Hence, for the probability map computation the brick is expanded into its neighbors: The expanded brick side length $s_e = \lfloor e \cdot s \rfloor$ is larger than the original brick by a factor $e > 1$. Let $h \in H := \mathbb{R}^{s_e^3}$ be a brick neighborhood, and $\text{nh}: N \rightarrow H$ and $\text{ctr}: H \rightarrow B$ be retrieval and center brick extraction functions, respectively. Then continuous labels ($\text{cl}: N \times L \rightarrow L$) are added at the border ($\text{brd}: H \rightarrow L$) of the expanded brick, where the probability values are (up-) sampled ($\text{smp}: N \times (\mathbb{R}^3 \rightarrow \mathbb{R}^3) \rightarrow H$) from the neighborhood of the parent node and its neighbors (where output probabilities $\mathcal{H}(\mathcal{P}(n), l)$ were already computed in a previous step).

$$\begin{aligned} \text{smp}(n, t)[p] &= \text{nh}(n)[t(p)] \\ \text{brd}(h) &= \{(p, h[p]) \mid \{p_x, p_y, p_z\} \cap \{0, s_e - 1\} \neq \emptyset\} \\ \text{cl}(n, l) &= \begin{cases} \emptyset & \mathcal{P}(n) = \epsilon \\ \text{brd}(\text{smp}(\mathcal{H}(\mathcal{P}(n), l), \mathcal{T}_{\mathcal{P}(n)} \circ \mathcal{T}_n^{-1})) & \text{else} \end{cases} \end{aligned}$$

User-defined labels are rasterized into the expanded brick and can thus directly influence the foreground probability map of the original brick. The probability map for the original brick is the s^3 -sized center of the expanded result. Equation 1 can thus be completed to apply to all nodes:

$$\text{br}(\mathcal{H}(n, l, \beta)) = \text{ctr}(\text{rw}(\text{nh}(n), \mathcal{T}_n(l) \cup \text{cl}(n, l), \beta)) \quad (2)$$

A large factor e is advantageous due to the increased high resolution global context, but also results in an increase of computational time by a factor of $\mathcal{O}(e^3)$. We suggest $e = 1.25$ as a balance between accuracy and run time.

C. Adaptive Parameter Setting

A challenge (but also advantage) of the octree data structure is that noise on the full resolution level is reduced by the mean filtering in the construction of coarser levels. While reduced noise on coarser octree levels is obviously advantageous for application of the random walker method, it also implies that the optimal choice for β is dependent on the octree level. Hence, an automatic way of computing suitable parameters is required. This has the additional advantage that β can be adapted to regions with different noise levels within the image as well. Bian et al. [26] assume additive Gaussian noise and first estimate the global variance σ^2 based on the intensity difference between the original image and estimated true intensities (obtained using a median filter f). Then β is defined to normalize the (estimated true) intensity difference of two neighboring voxels by the estimated variance of intensity differences $\sigma_d^2: H \rightarrow \mathbb{R}$ (which uses σ^2 and f): $\beta_n = (2\sigma_d^2(\text{nh}(n)))^{-1}$. Equation 2 is thus further refined to use a β_n dependent on the current node:

$$\text{br}(\mathcal{H}(n, l)) = \text{ctr}(\text{rw}(\text{nh}(n), \mathcal{T}_n(l) \cup \text{cl}(n, l), \beta_n)) \quad (3)$$

Additionally, as β_n normalizes the estimated true voxel intensities, the edge weight function is modified to operate on $f(b)$: $w_{p,q} = \exp(-\beta_n(f(b)[p] - f(b)[q])^2)$.

The above method can be generalized to other noise models [45]. For datasets with Poisson noise (for example those in our real world data evaluation), the following edge function is used: $w_{p,q} = \exp(-\frac{1}{2}(\sqrt{b[p]} - \sqrt{b[q]})^2)$.

D. Run Time Enhancements

While the preliminary framework description above (Equation 3) ensures accuracy and constant memory complexity, this section discusses run time enhancements that directly follow (iterative solver initialization, parallelization) or are enabled by the algorithm structure (pruning).

1) *Pruning*: When labeling objects larger than at least one brick (which is also the case when only labeling relatively few, small foreground objects, leaving large background regions) it is often unnecessary to complete the proposed procedure down to the leaf level for all branches of the tree. When the resulting foreground probability B of a node is *homogeneous* ($\text{hom}: B \rightarrow \text{Bool}$), i.e., its range is smaller than a threshold t_{hom} , its children do not have to be processed.

$$\text{hom}(b) = \left(\max_{p \in \{1, \dots, s\}^3} b[p] - \min_{p \in \{1, \dots, s\}^3} b[p] \right) < t_{hom}$$

In our experiments the threshold was set to $t_{hom} = 0.3$. Furthermore, if the user is not interested in the foreground probability volume itself, but in a binary segmentation (by thresholding the probability at $p = 0.5$), nodes do not have to be processed further if the foreground/background state is already determined ($\text{dt}: B \rightarrow \text{Bool}$). This is the case if the lowest foreground probability is above 0.5 (resulting in a brick) or the maximum is below 0.5 (resulting in a foreground brick) by a specific margin t_{bin} .

$$\begin{aligned} \text{dt}(b) = & \min_{p \in \{1, \dots, s\}^3} b[p] - 0.5 > t_{bin} \\ & \vee 0.5 - \max_{p \in \{1, \dots, s\}^3} b[p] > t_{bin} \end{aligned}$$

For a binary segmentation (i.e., the output probability map thresholded at 0.5) a low value of $t_{bin} = 0.01$ is sufficient.

This pruning process may cause sampling probabilities for continuous labels at the border of the current brick to fail for neighbors of the parent node since the tree is no longer complete. In this case sampling continues at the nearest transitive parent of the absent node, in the worst case at the root node. Additionally, during the rasterization foreground and background labels may be in conflict ($\text{cfl}: N \times L \rightarrow \text{Bool}$), i.e., occupy the same voxel:

$$\begin{aligned} \text{cfl}(n, l) = & \exists (q_0, p_0), (q_1, p_1) \in l : \\ & [\mathcal{T}_n(q_0)] = [\mathcal{T}_n(q_0)] \wedge p_0 \neq p_1 \end{aligned}$$

In this case the voxel is left unlabeled and its output probability is determined by other non-conflicting labels. While this is normally not a problem on the leaf level (i.e., original resolution of the volume) for sensible user-defined labels, non-conflicting labels on the finest level can be in conflict when rasterized on a coarser octree level with a lower brick resolution. In the core procedure this is not problematic since the ambiguity is automatically resolved at a finer level. For pruning this means that children of nodes with label conflicts cannot be pruned and thus have to be processed even if they appear to be homogeneous or determined.

With the above definitions we can define \mathcal{H}_p as an optimized version of \mathcal{H} (from Equation 3):

$$\begin{aligned} \text{pruneable}(b) &= \text{hom}(b) \vee \text{dt}(b) \\ \mathcal{H}_p(n, l) &= \begin{cases} \epsilon & \text{pruneable}(\mathcal{H}(n, l)) \wedge \neg \text{cfl}(n, l) \\ \mathcal{H}(n, l) & \text{else} \end{cases} \end{aligned}$$

If foreground and background can clearly be separated in the image (and thus no regions of high uncertainty are generated in the output probability map), the pruning methods described above make sure that only children of bricks that intersect the object surface (i.e., the foreground/background boundary) need to be processed. For a “well behaved” object surface (i.e., with finite surface area, which is of course always the case in a discretized image) the number of bricks that intersect the object boundary is within $\mathcal{O}(k^{\frac{2}{3}})$ if the volume is subdivided into k bricks. A proof of this statement can be found in the appendix. As the size of a brick is constant and computations performed on the brick are thus within $\mathcal{O}(1)$, the total runtime of the algorithm is within $\mathcal{O}(v^{\frac{2}{3}})$ for a volume of $v = d_x \times d_y \times d_z$ voxels. This behaviour is also observed experimentally in section V.

2) *Iterative Solver Initialization*: As noted by Grady [8], the system of linear equations is often efficiently solved using an iterative method [44], which can typically be accelerated by providing an initial state that is close to the true solution. For all but the root level this is the case in our method: As pointed out above, the foreground probability map computed for the parent brick of any node can be sampled to provide an approximation of the solution for the current level. This approximation is thus also used as an initialization for the iterative solver.

3) *Parallelization*: As all bricks within an octree layer are independent from one another, the computation can trivially be parallelized. While costly brick processing steps (such as filtering, edge weight computation and solving of linear equation systems) are parallelizable themselves, this makes the procedure well suited for parallelization on multiple GPUs in workstations.

E. Incremental Labeling

The set of user-defined seeds in semi-automatic segmentation algorithms is typically not created in a single step, but built up incrementally in an evaluate-edit-compute cycle, in which the user inspects the existing segmentation, changes the parameters (seeds) of the algorithm and then waits for the algorithm to update the segmentation before starting the cycle again, inspecting the updated segmentation [46]. As such, computation time is not the only factor affecting the total time to produce the desired segmentation result, but still very important, since high latency between user interaction and display of intermediate results impacts user performance [47]. Consequently, the *incremental run time* of an algorithm, in which the previous result is an additional input, has to be considered and evaluated.

Grady [8] suggests using the previous result as initialization for iterative solver for the standard random walker method. This is applicable here (even for non-iterative application, as

described above), but not sufficient if the previous result octree is nearly complete: In this case operations such as loading (possibly from disk) and edge weight computations still have to be executed for all branches of the tree. Instead, we reuse entire branches of the previous result if they can be expected to be similar to the new result: After computing a new foreground probability map for a node if the result is sufficiently similar to the previous probability map of the corresponding node in the old tree, the new node is discarded and replaced by the old node *including* its children. With $\mathcal{H}_{it}(n, l')$ as the previous solution for label set l' :

$$\mathcal{H}_{it}(n, l) = \begin{cases} \mathcal{H}_{it}(n, l') & \text{br}(\mathcal{H}_{it}(n, l')) \approx \text{br}(\mathcal{H}(n, l)) \\ & \wedge \neg \text{cfl}(n, l) \\ \mathcal{H}(n, l) & \text{else} \end{cases}$$

Similar to pruning, if there are conflicts in the set of (changed) labels affecting this brick, this optimization cannot be performed, but it is sufficient to consider conflicts where at least one of the recently added labels ($l - l'$) is involved. Pruning and incremental labeling can of course be combined. Probability maps are considered similar if the maximum pairwise difference is below a threshold t_{inc} . We set $t_{inc} = 0.01$ in all experiments.

$$b_0 \approx b_1 \Leftrightarrow \max_{p \in \{1, \dots, s\}^3} (|b_0[p] - b_1[p]|) < t_{inc}$$

V. EVALUATION AND DISCUSSION

As stated previously, the goal of the proposed framework is to greatly reduce the required runtime while maintaining a high segmentation quality. This is evaluated in this section in the following way: First, the framework is compared to the baseline method using the public CT-ORG [48] dataset. Then, as the CT-ORG dataset does not contain datasets far exceeding main memory, the proposed method is additionally evaluated using synthetic data which allows for fine grained control over volume sizes and also enables simulation of incremental labeling. Afterwards, the applicability of the method to large real world data is shown in a small case study using datasets from current biomedical research [49] of up to 377 GB in size (where the baseline method is not applicable). Finally, we analyze the importance and influence of the introduced pruning methods using synthetic and real data. All experiments and the case study were carried out on a standard PC with an Intel i5-6500 (3.2 GHz, 4 core), 16 GB RAM, a single Nvidia GTX 1060 (6 GB RAM) and a Samsung EVO 970 SSD.

A. Real World CT Data

In order to compare the segmentation accuracy of the proposed framework to the basic method on real world data, we used the CT-ORG dataset [48], which includes 140 scans in total with associated ground truth segmentation for up to 6 organs types. In order to not exceed the memory capacity of the graphics card when using the regular random walker method, scans were cropped to a 350^3 voxel region around each organ before evaluation. Scans with less than 350 slices were left out for simplicity, which results in around 80 datasets for each organ except for the brain class, which in general is

not visible in most scans in the database. 50 foreground and 200 background seeds were generated by randomly sampling voxel positions from the foreground and background regions.

The results are summarized in Table I where statistically significant differences are highlighted in bold (sample distributions were compared with the Wilcoxon signed-rank test ($\alpha = 0.01$) and Holm-Bonferroni correction for the 12 tests). As expected, for all organs, the proposed hierarchical method is clearly faster than the basic method, specifically by two orders of magnitude for datasets of 350^3 voxels: The basic method requires between 3 and 4 minutes while the hierarchical method finishes after 1 to 6 seconds. In all but one (brain dataset with only 7 samples) cases this difference is statistically significant.

Looking at the achieved dice score, it can be seen that overall the method achieves the goal of maintaining a high segmentation quality when compared to the regular method: For brain and liver, the difference in dice score is not statistically significant. For bone, the proposed method shows a statistically significant and substantially better dice score (0.40 vs. 0.72 in the mean). In the case of the bladder, lungs and kidney segmentations, the regular method achieves better results with statistical significance. It is however of note that the mean dice score of the proposed method is not drastically worse for bladder and kidneys and actually only differs by 0.005 for lungs (0.964 vs. 0.959). We therefore conclude that the proposed method is actually a reasonable approximation to the basic method and can even achieve substantially better results, especially in cases where the basic method does not score well.

Having confirmed the expected run time and accuracy characteristics on real world data, in the next section we will expand the evaluation using synthetic data which allows full control over dataset sizes and thus observation of trends in both accuracy and, importantly, run time scalability.

B. Synthetic Data

For systematic comparison with the basic approach on different scales, we generate a ground-truth volume (binary segmentation), a noisy input volume (with a mean of 0.3/0.7 for background/foreground and additive Gaussian noise with varying σ), as well as foreground and background labels defined as points. Foreground structures cover 1% of the total volume. The *structure size* range is a parameter that influences the size of individual foreground objects and is relative to the dataset size. The upper bound (*structure size* in the following) is 10% if not specified otherwise. The lower bound is always half of the *structure size*. Existing frameworks for biomedical test data generation [50] are limited in the size of datasets which can be generated. Therefore we define structures as described below and create a voxel representation by organizing the primitives (spheres, cylinders) in sorted queues (according to their bounding boxes) for the z , y and x -dimension, scanning the output volume linearly, for each voxel rasterizing active primitives [51]. We chose the following biomedical application-inspired scenarios:

Cells are represented as spheres with a diameter within structure size and placed randomly within the volume. Centers

TABLE I

ACCURACY AND RUN TIME PERFORMANCE COMPARISON OF THE REGULAR RANDOM WALKER METHOD [8] AND THE PROPOSED HIERARCHICAL VARIANT (USING THE REGULAR VARIANT AS A COMPONENT). WE REPORT THE MEAN AND STANDARD DEVIATION FOR THE TOTAL REQUIRED RUN TIME AND THE DICE SCORE WHEN COMPARED TO THE GROUND TRUTH SEGMENTATION. STATISTICALLY SIGNIFICANTLY BETTER RESULTS ARE HIGHLIGHTED IN BOLD. AS EXPECTED, THE PROPOSED OCTREE-BASED METHOD CLEARLY OUTPERFORMS THE BASELINE METHOD IN TERMS OF RUN TIME WHILE MAINTAINING HIGH SEGMENTATION QUALITY (AND EVEN OUTPERFORMING THE REGULAR METHOD IN ONE SIGNIFICANT CASE).

Organ	Number of Datasets	Run time (Regular)	Run time (Octree)	Dice Score (Regular)	Dice Score (Octree)
Liver	80	206.81s \pm 14.39s	4.36s \pm 1.10s	0.788 \pm 0.18	0.817 \pm 0.09
Bladder	77	208.94s \pm 11.74s	1.59s \pm 0.65s	0.705 \pm 0.18	0.619 \pm 0.19
Lungs	81	213.74s \pm 12.34s	5.18s \pm 2.33s	0.964 \pm 0.03	0.959 \pm 0.03
Kidneys	81	223.36s \pm 14.50s	1.88s \pm 0.45s	0.908 \pm 0.11	0.860 \pm 0.17
Bone	81	214.35s \pm 13.50s	4.00s \pm 0.64s	0.396 \pm 0.12	0.721 \pm 0.10
Brain	7	224.54s \pm 13.94s	1.04s \pm 0.15s	0.818 \pm 0.03	0.625 \pm 0.07

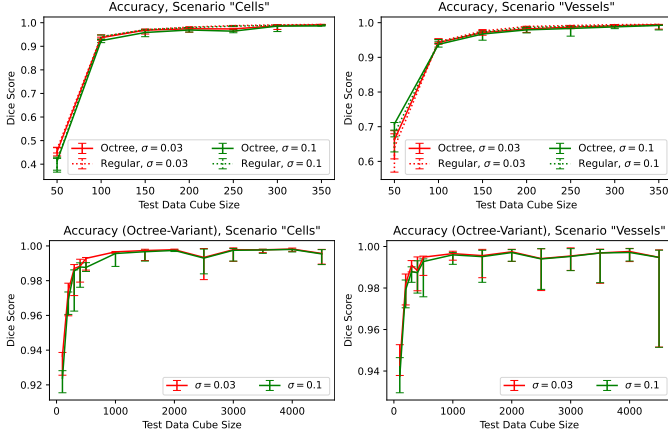


Fig. 3. Median Dice score of the generated segmentation compared to ground truth for regular random walker and octree variant (top row), and the octree variant for larger volume sizes (bottom row). Error bars show minimum/maximum scores.

of spheres do not intersect other spheres, thus reducing overlap, but allowing for “clustering” of cells. Foreground seeds are placed at the center of each sphere. For each generated sphere 2 background seed points are placed at a random position with a distance of two radii from the cell center, but outside of any other cell.

Vessels consist of segments of cylindrical shape and spheres at branching points. Each vessel tree starts with a radial diameter within the structure size from a random point at the volume border. The vessel branches at $5 \times$ radius into two segments, preserving cross-section area. This process repeats recursively. Two points along the vessel centerline are added to the set of foreground labels while two corresponding points outside the vessel with a distance of twice the radius are added as background labels.

All experiments have been executed 5 times with different seeds for the random number generator so that minimum, median and maximum performance (both in terms of accuracy and run time) can be evaluated in the following.

1) *Accuracy*: To evaluate the accuracy of the regular and hierarchical variant, the generated segmentation (using a threshold of 0.5 on the foreground probability map) was compared to the ground truth segmentation using the Dice score. First, we review results for low noise levels ($\sigma = 0.03$, with a resulting overlapping coefficient [52] between foreground and

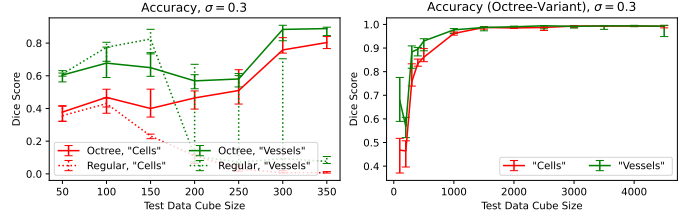


Fig. 4. Median Dice score of the generated segmentation compared to ground truth for high noise levels ($\sigma = 0.3$). Error bars show minimum/maximum scores.

background intensity distributions (i.e., the overlapping area of the density functions) of roughly 10^{-11}) where the foreground and background intensity distributions are largely separate, and for medium noise levels ($\sigma = 0.1$, overlap coefficient 0.046) where the distributions overlap moderately.

Figure 3 (top row) compares the accuracy of the basic random walker [8] to the proposed octree variant (using the regular variant [8] as a component) on synthetic datasets up to a volume size of $350 \times 350 \times 350$. Larger volumes could not be processed by the regular variant due to limited graphics memory. The bottom row hence only shows the octree variant, up to a volume size of $4500 \times 4500 \times 4500$ voxels (182 GB).

At these low and medium noise levels regular and octree variant yield similar results. Here, the Dice score increases for larger volume sizes and is above 0.9 for sizes larger than 50. Both the increase and low score for a volume size of 50 can be explained by the median filter applied during the adaptive parameter setting which disturbs the border of objects. This effect is reduced when the resolution (i.e., volume size) increases. For datasets larger than 500^3 voxels, the minimum Dice score of the octree variant does not drop below 0.95 and in the median stays above 0.995.

It should further be noted that differences between both noise levels appear to reduce as the resolution is increased. This motivates the extension of the above comparison to high noise levels ($\sigma = 0.3$) where foreground and background intensity distributions overlap to a large degree (overlapping coefficient [52] of 0.50). Dice scores for small volumes and both variants (left) as well as for large volumes and the hierarchical method are shown in Figure 4. It is apparent that both variants struggle to produce the expected result for small volume sizes due to the extreme noise. This is especially true for the cell scenario, possibly due to fewer seeds points from

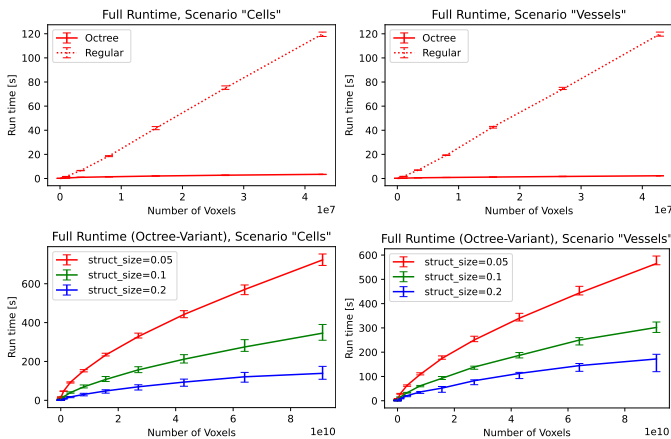


Fig. 5. Median wall-clock run time of the regular random walker and proposed octree variant (top row), and octree variant for larger volume sizes and varying structure sizes (bottom row). Error bars show minimum/maximum run times.

the dataset generation. However, while the regular random walker variant produces increasingly bad scores volumes larger than 150^3 voxels, the hierarchical variant generates relatively consistent results until it starts to improve at a volume size of roughly 300. For volumes with more than 1000^3 voxels Dice scores consistently above 0.95 are achieved. The mean filtering of the LOD approach can be expected to reduce the (additive) noise at the coarser levels of the pyramid, allowing the broad structure of foreground objects to be captured, even when the exact surface features cannot be reconstructed due to the noise.

2) *Full Run Time*: Figure 5 (top row) compares the run time of the basic random walker [8] to the proposed octree variant (using the regular variant [8] as a component) on synthetic datasets up to a volume size of $350 \times 350 \times 350$. The bottom row only shows the octree variant, up to a volume size of $4500 \times 4500 \times 4500$ voxels (182 GB). In direct comparison, the octree variant is considerably faster than the regular random walker. This becomes even more apparent for increasing dataset sizes. For 350^3 voxel datasets the original variant requires roughly two minutes of computation time (independent of the scenario) while the proposed method completes in less than 4s in all cases. Furthermore, while the run time of the regular approach is shown to be linear, the run time of the proposed framework appears sub-linear (looking at the bottom row of Figure 5). This is consistent with the runtime behavior predicted in subsection IV-D1: Due to pruning, at any level only bricks intersecting a foreground-background boundary within the volume require further processing (in assumed perfect conditions), ultimately resulting in a runtime of $v^{2/3}$ for a volume of v voxels. This hypothesis is further supported by the fact that smaller structure sizes (resulting in a *higher number* of structures and ultimately more surface area) cause longer computation times.

3) *Run time with Simulation of Incremental Labeling*:

In order to demonstrate run time savings of the incremental labeling aspect of the proposed approach, two subsequent runs are performed to simulate a single user editing step. In the first run, a randomly selected foreground label (a single centerpoint

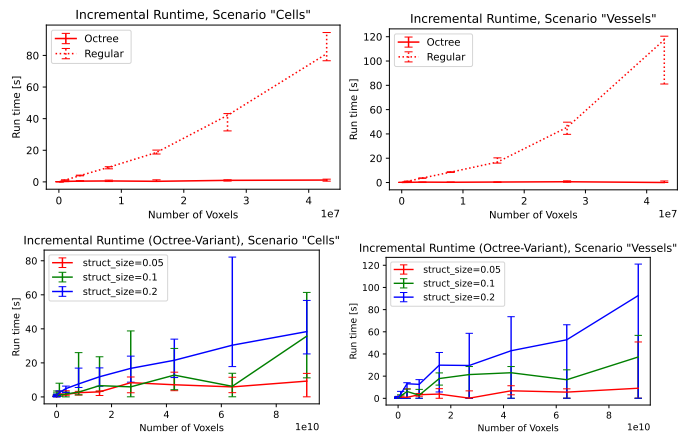


Fig. 6. Median wall-clock run time after adding a label for a previously unlabeled foreground component for regular random walker and octree variant (top row), and for the octree variant with larger volume sizes and varying structure sizes (bottom row). Error bars show minimum/maximum run times.

of a sphere or a vessel segment) is retained from the complete set of labels. For the second run this label is added and the run time is measured.

Figure 6 shows the incremental run time for the regular and octree random walker approach in comparison (top row), and for the octree variant for datasets larger than 350^3 voxels (bottom row). Both appear to benefit from the additional information of a previous solution. Specifically, for the regular random walker variant, at 300^3 voxel the average run time is reduced from roughly 80 to roughly 40 seconds. However, a super-linear median run time can be observed and especially for larger dataset sizes the runtime is still orders of magnitude higher than the time the hierarchical variant requires. The proposed hierarchical variant shows moderate increase in computation time from less than 100 milliseconds for the smallest dataset (50^3 voxels) to consistently less than 2 seconds for the 350^3 voxel dataset, which is a further reduction in comparison with the full (non-incremental run time) shown in Figure 5.

In contrast to the full run time evaluation, structure sizes have a different effect: The overall trend is that larger structure sizes require more computation time. This is expected, as (in contrast to the full computation) only a single structure element requires modification. Smaller structures thus require less work overall. For a structure size of 0.05, the hierarchical method completes in a median time of 10 seconds, even for datasets of 4500^3 voxels (182 GB). Larger structures (structure size 0.2, spanning large portion of volume), result in higher processing times up to roughly 40 seconds (cells) and 90 seconds (vessels) in the median and 80 seconds (cells) and 120 seconds (vessels) in the maximum. This is significantly lower than for the full computation and still usable in practice considering that volumes with large structures likely require few labels overall. The accuracy of both the regular and octree approach were observed to be equivalent to non-incremental runs.

TABLE II

INFORMATION ABOUT THE PROCESSED REAL WORLD DATASETS INCLUDING FULL RUN TIME (WITHOUT PREVIOUS RESULTS AND WITH THE FULL LABEL SET) AND TIME RANGES FOR LABEL UPDATE OPERATIONS.

Dataset	Voxel Dimensions	Real Dimensions	Size	Full Run Time	Incr. Run Time
Kidney Vasculature (Subset)	$5153 \times 4791 \times 1213$	$3.9 \times 3.6 \times 3.6 \text{ mm}^3$	60 GB	10 min	1 s–15 s
Kidney Vasculature (Full)	$9070 \times 12732 \times 1634$	$6.8 \times 9.6 \times 4.9 \text{ mm}^3$	377 GB	11 min	1 s–60 s
Full Kidney (Full)	$9070 \times 12732 \times 1634$	$6.8 \times 9.6 \times 4.9 \text{ mm}^3$	377 GB	48 min	4 min–48 min
Brain Vasculature	$3895 \times 4215 \times 1801$	$6.3 \times 6.8 \times 3.6 \text{ mm}^3$	59 GB	7 min	1 s–17 s

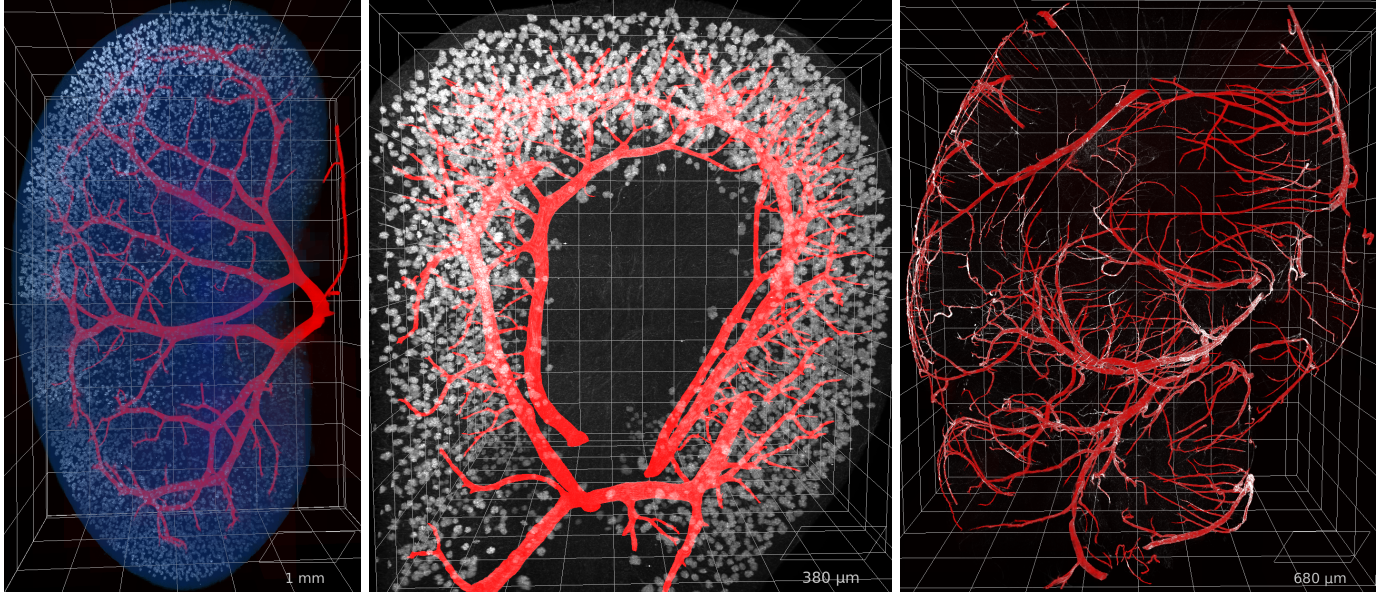


Fig. 7. Raycasting rendering of the kidney dataset (377 GB left, 60 GB center) mainly showing high intensity glomeruli (grayscale) and of the brain dataset (59 GB, right), including the arterial vessel tree (red) and kidney volume (blue) segmentation obtained using the proposed method. The resulting vessel networks have a total length of 164 mm (left), 170 mm (center), 428 mm (right) and a volume of 0.67 mm^3 (left), 0.35 mm^3 (center) and 0.32 mm^3 (right).

C. Small Case Study: Large Real Data

In the previous two subsections we have shown that the proposed hierarchical variant of the random walker method is comparable to the basic method in accuracy and that it has substantial benefit in terms of the required computational time and memory requirements.

Here, as part of a small case study, we additionally apply the proposed method to real multi-gigabyte datasets far exceeding the limits of available main memory that are used in current biomedical research [49] where the baseline method is not applicable (due to the massive data size). Comparison with ground truth data can not be performed in this case since ground truth information is not available – at least in part due to the lack of labeling tools capable of handling data of this size, a gap that our work aims to fill. The processed datasets include an antibody-stained light sheet microscopy scan of a mouse kidney and a scan of a mouse brain hemisphere². In total 4 labeling tasks were carried out: 1) A binary segmentation of the arterial vasculature (up to the capillary level) created on

a 60 GB subset of the whole kidney dataset; 2) The vascular tree of the full 377 GB kidney dataset up to a vessel diameter of about $10 \mu\text{m}$ and 3) a foreground mask for the whole kidney volume were created in the same way; 4) The vasculature of the 59 GB brain dataset up to a vessel diameter of roughly $10 \mu\text{m}$ was created similarly. Figure 7 shows a rendering of the original kidney dataset, in conjunction with the vasculature and whole kidney segmentation for illustration (left), a subset of the kidney dataset with a more detailed segmentation of the vasculature (center) and the brain dataset with the vasculature segmentation (right).

Table II shows some additional information about the datasets, including the full computation time (without a previous result, given the full set of labels) and observed computation time ranges for updates to the label set. The observed full computation time is in line with the results of the synthetic dataset experiments (see Figure 5) and thus substantial, but satisfactory in practice (below one hour) given the size of the datasets. For vasculature the incremental computation times are observed to be in the order of seconds (especially for smaller vessels (1s), but also for the long sections of the largest vessels (60s)) and are thus dominated or roughly equivalent to the time a user needs for inspection and interaction with the data. For the full kidney segmentation individual changes

²All procedures involving animals (i.e., procedures performed to obtain these datasets) were carried out in strict accordance with the German animal protection legislation (Tierschutzgesetz und Tierschutzversuchstierverordnung). The protocol was approved (84-02.04.2016.A218) by the Committee on the Ethics of Animal Experiments of the Landesamt für Natur, Umwelt und Verbraucherschutz (LANUV).

to the label set require a longer run time to update the output probability map (between few minutes and the full run time) in this experiment. This, however, is balanced out by the fact that very few labels are required overall. In general, regions of high uncertainty (i.e., foreground probability values around 0.5) cause longer computation times since those regions often cannot be pruned. This was also the case for the kidney, where three foreground labels in the center and two on the outside were able to cleanly separate foreground from background at the capsule, but failed to define a clear boundary at the hilum where vessels are entering the kidney. Here, a number of additional labels were required to remove the ambiguity. Thus, a sudden increase of computation time signifies resulting uncertainty in the segmentation and may prompt to correct the last set of labels and restart the computation.

The total label time (including user interaction) was roughly three hours for the large vasculature in the full 377 GB dataset, and about seven hours for the 60 GB subset as well as the 59 GB brain dataset, both with substantially more detail. The broad majority of this time can be attributed to the user interaction and identification of vessels itself, which is especially challenging for the kidney datasets since segmented vessels are often of comparatively low intensity, which also makes the application of fully automated method difficult. The Kidney segmentation is dominated by the whole compute time since the initial set of labels already generated a good segmentation of the whole kidney and few corrections were required. The user interaction time itself was in the order of minutes.

D. Influence of Pruning Methods

Apart from the reduced memory footprint, the hierarchical processing scheme introduced in this paper may not by itself bring large advantages in terms of total runtime. This is achieved by pruning branches of the probability map octree during its construction based on the criteria *hom* (homogeneity based) and *dt* (pruning of already determined complete foreground or background regions). In this section we will determine the influence of both methods by observing results when disabling one of two or both pruning methods. For both pruning methods the thresholds suggested in section IV were applied ($t_{hom} = 0.3$ and $t_{bin} = 0.01$).

Table III shows the mean runtime and dice score when applying the method to the same CT datasets as in subsection V-C. The pruning methods appear to have a negligible influence on the segmentation accuracy: The difference in dice score is less than 1% between any of the examined configurations. Both pruning methods reduce the overall runtime when applied on their own: *hom*-based pruning roughly halves the full runtime in comparison to no pruning, while *dt*-based pruning reduces the time to almost a quarter. Combining both pruning methods yields the same speedup as only applying *dt*-based pruning.

A similar evaluation was also conducted for a total of 40 artificial datasets, constructed as described in subsection V-B with 20 datasets from both scenarios. All datasets consist of 1000^3 voxels with a structure size of 10%. The results in

TABLE III
MEAN DICE SCORE AND RUNTIME ON THE CT-ORG REAL WORLD DATA SETS FOR DIFFERENT COMBINATIONS OF PRUNING METHODS: HOMOGENEITY-BASED PRUNING (ACCORDING TO *hom*) AND PRUNING OF ALREADY DETERMINED BRANCHES (ACCORDING TO *dt*).

hom-Pruning	dt-Pruning	Runtime	Dice Score
No	No	12.88s	0.7939
Yes	No	5.99s	0.7942
No	Yes	3.36s	0.7937
Yes	Yes	3.37s	0.7940

TABLE IV
MEAN DICE SCORE AS WELL AS FULL AND INCREMENTAL RUNTIME (RT) ON 40 SYNTHETIC DATASETS FOR DIFFERENT COMBINATIONS OF PRUNING METHODS: HOMOGENEITY-BASED PRUNING (ACCORDING TO *hom*) AND PRUNING OF ALREADY DETERMINED BRANCHES (ACCORDING TO *dt*).

hom-Pruning	dt-Pruning	Full RT	Incr. RT	Dice Sc.
No	No	292.27s	18.54s	0.9960
Yes	No	16.61s	2.30s	0.9949
No	Yes	16.18s	2.26s	0.9941
Yes	Yes	16.20s	2.23s	0.9941

Table IV are overall similar to the results on the CT dataset: The dice score differs by no more than 1% and both pruning methods exhibit a substantial speedup for a full run when compared to running without pruning. Here, there is very little difference in speedup between both pruning methods on their own (roughly by a factor of 17-18). Once again, combining both pruning methods does not result in an additional speedup. It should be noted however, that – as described in section IV – *dt*-based pruning only makes sense if the desired end result is a binary segmentation. If on the other hand the foreground probability map (for example for uncertainty visualization) is desired, it may be useful to only apply homogeneity-based pruning which still achieves a considerable speedup on synthetic and real data.

Table IV also shows that the reusing of branches for incremental labeling (when adding a single foreground label in this experiment) results in a substantial speedup even when not pruning branches (roughly by a factor of 16). At the same time, applying any of the two or both pruning methods further reduces the incremental runtime to 12-13% of the runtime without pruning.

VI. CONCLUSION

We have presented a scalable approximation of the random walker method for semi-automatic segmentation of very large volumetric datasets. It can be applied to volumes that exceed the main and graphics memory capacity and outperforms the original variant in run time performance while approximating the original method well on both artificial and real test sets. While the original random walker method fails to process datasets larger than a few hundreds of megabytes due to memory exhaustion, here the applicability to large real world datasets of up to 377 GB has been demonstrated in a case study which also confirmed the runtime behavior observed on controlled synthetic test data. The approach can process large datasets on consumer PCs, but at the same time is future-proof and scalable beyond the experiments in this paper, as

it is easily parallelizable and should be able to fully utilize multi-GPU setups. As such, it should be useful, for example, as a stage in a pipeline for quantitative analysis of large volumetric datasets, or as a highly efficient labeling tool for machine learning applications. An implementation of the presented method has been published as part of version 5.2 of Voreen [53], a widely used open source volume rendering and processing framework.

In the future, we will explore the integration of extensions to random walker algorithm [9] (such as automatic label generation [24]). We will further improve the current implementation by moving more computations, such as pre-processing (median filter, adaptive parameters) and linear equation system construction, from the CPU onto the GPU, thus further improving the scalability. Furthermore, it is worth investigating the use of other compatible methods that compute segmentation probability maps from user-defined seeds in our framework that is of general nature.

APPENDIX

A PROOF FOR $\mathcal{O}(B^{\frac{2}{3}})$ GROWTH OF THE NUMBER OF BRICKS INTERSECTING THE OBJECT SURFACE

Definitions: Let $P = [0, N] \times [0, M]$ be a parameter space and let $V = [0, 1]^3 \subset \mathbb{R}^3$ define a cubic volume in 3D. $\phi : P \rightarrow V$ defines the surface of a foreground object in V using the parameter space P . We restrict ϕ to be able to “squish” the surface, but not “stretch” it, i.e.,

$$\forall x, y \in P : \|x - y\|_2 \geq \|\phi(x) - \phi(y)\|_A \quad (4)$$

where $\|\cdot\|_A$ denotes the distance on the surface A . In practice this is not a limitation, since P can be chosen as large as required in order for ϕ to only “squish”.

For V we define a grid-like subdivision into $n^3 =: B$ cubic bricks C_{klm} (i.e., L_∞ balls) of side length $d \times d \times d$, with $d = \frac{1}{n}$ and $(k, l, m) \in \{1, \dots, n\}^3 =: I$. These bricks C_{klm} completely cover V , i.e.: $\bigcup_{s \in I} C_s = V$. In particular this means that the centers c_{klm} of bricks C_{klm} have the following L_∞ -distance relationship:

$$\begin{aligned} \forall (k, l, m), (k', l', m') \in I : \|c_{k,l,m} - c_{k',l',m'}\|_\infty \\ = \max(|d(k - k')|, |d(l - l')|, |d(m - m')|) \\ \stackrel{d > 0}{=} d \max(|k - k'|, |l - l'|, |m - m'|) \end{aligned} \quad (5)$$

We can count the number of bricks that intersect with the surface A with the following function $b(A)$:

$$b(A) = |\{r \in I \mid C_r \cap A \neq \emptyset\}|$$

Statement: The number of bricks that intersect the object surface A grows with the $\frac{2}{3}$ of B , i.e.: $b(A) \in \mathcal{O}(B^{\frac{2}{3}})$.

Proof: The euclidean distance between two points on the surface $A = \phi(P)$ is bounded by the surface distance, i.e.:

$$\begin{aligned} \forall x, y \in P : \|\phi(x) - \phi(y)\|_A \geq \|\phi(x) - \phi(y)\|_2 \\ \stackrel{\text{Equation 4}}{\Rightarrow} \|x - y\|_2 \geq \|\phi(x) - \phi(y)\|_2 \end{aligned} \quad (6)$$

Similar to the grid-subdivision of V , we divide the parameter space P up into $p \cdot q$ squares, where $p = \frac{N}{d} = Nn, q =$

$\frac{M}{d} = Mn$ and squares S_{ij} (i.e. L_∞ -balls) of size $d \times d$ with $i \in \{1, \dots, p\}, j \in \{1, \dots, q\}$. Without loss of generality let $N, M \in \mathbb{N}$ and thus also $p, q \in \mathbb{N}$. If this is not the case, we can simply replace $\phi_{new} = c \circ \phi$ with an element-wise scaling function c . Let s_{ij} be the center of the L_∞ -ball S_{ij} . Then, a point from S_{ij} has euclidean distance of less than d to s_{ij} after application of ϕ :

$$\begin{aligned} \forall x \in S_{ij} : \|\phi(x) - \phi(s_{ij})\|_2 &\stackrel{\text{Equation 6}}{\leq} \|x - s_{ij}\|_2 \\ &\stackrel{\dim(P)=2}{\leq} \sqrt{2} \|x - s_{ij}\|_\infty \stackrel{x \in S_{ij}}{\leq} \sqrt{2} \frac{d}{2} = \frac{d}{\sqrt{2}} < d \end{aligned} \quad (7)$$

Now, let $x \in S_{ij}$ and $\phi(s_{ij}) \in C_u$ and $\phi(x) \in C_t$. Then, using the triangle inequality, we can find a strict upper bound for the distance between the centers of the bricks of $\phi(x)$ and $\phi(s_{ij})$:

$$\begin{aligned} &\|c_u - c_t\|_\infty \\ \leq &\|c_u - \phi(s_{ij})\|_\infty + \|\phi(s_{ij}) - \phi(x)\|_\infty + \|\phi(x) - c_t\|_\infty \\ &\stackrel{\phi(s_{ij}) \in C_u \wedge \phi(x) \in C_t}{\leq} \frac{d}{2} + \|\phi(x) - \phi(y)\|_\infty + \frac{d}{2} \\ \leq &\frac{d}{2} + \|\phi(x) - \phi(y)\|_2 + \frac{d}{2} \stackrel{\text{Equation 7}}{<} \frac{d}{2} + d + \frac{d}{2} = 2d \end{aligned} \quad (8)$$

Hence, we know that the index difference $u - t = (k', l', m') \in \mathbb{Z}$ of the brick of $\phi(s_{ij})$ (C_u) and the one that contains $\phi(x)$ (C_t) is restricted:

$$\begin{aligned} d \max(|k'|, |l'|, |m'|) &\stackrel{\text{Equation 5}}{\leq} \|c_u - c_t\|_\infty \stackrel{\text{Equation 8}}{<} 2d \\ &\Rightarrow |k'| < 2 \wedge |l'| < 2 \wedge |m'| < 2 \\ &\stackrel{k', l', m' \in \mathbb{Z}}{\Rightarrow} k', l', m' \in \{-1, 0, 1\} \end{aligned} \quad (9)$$

Let $I_u = \bigcup_{(k', l', m') \in \{-1, 0, 1\}} u + (k', l', m')$ be set of indices of bricks that intersect with the patch $\phi(S_{ij})$. Then we can show that the surface patch $\phi(S_{ij})$ is contained in a (connected) region of at most $|\{-1, 0, 1\}^3|$ bricks:

$$\begin{aligned} b(\phi(S_{ij})) &= |\{r \in I \mid C_r \cap \phi(S_{ij}) \neq \emptyset\}| \\ &= |\{r \in I_u \mid C_r \cap \phi(S_{ij}) \neq \emptyset\}| \\ &\quad \cup \{r \in I \setminus I_u \mid C_r \cap \phi(S_{ij}) \neq \emptyset\}| \\ &\stackrel{\text{Equation 9}}{=} |\{r \in I_u \mid C_r \cap \phi(S_{ij}) \neq \emptyset\}| \\ &\leq |I_u| = 27 \end{aligned} \quad (10)$$

With this information, we can find an upper bound for $b(A)$

$$\begin{aligned}
b(A) &= |\{r \in I \mid C_u \cap \bigcup_{ij} \phi(S_{ij}) \neq \emptyset\}| \\
&= |\{r \in I \mid \bigcup_{ij} (C_u \cap \phi(S_{ij})) \neq \emptyset\}| \\
&= |\{r \in I \mid \bigvee_{ij} (C_u \cap \phi(S_{ij})) \neq \emptyset\}| \\
&= |\bigcup_{ij} \{r \in I \mid C_u \cap \phi(S_{ij}) \neq \emptyset\}| \\
&\leq \sum_{ij} |\{r \in I \mid C_u \cap \phi(S_{ij}) \neq \emptyset\}| \\
&= \sum_{ij} b(\phi(S_{ij})) \stackrel{\text{Equation 10}}{\leq} \sum_{ij} 27 \\
&= \sum_{i \in \{1, \dots, p\}} \sum_{j \in \{1, \dots, q\}} 27 = 27pq \\
&= 27NMn^2 = 27NMB^{\frac{2}{3}} \in \mathcal{O}(B^{\frac{2}{3}})
\end{aligned}$$

since N and M are constants for a given parametrization ϕ and surface $A = \phi(P)$. ■

If the surface of the object is not a single connected component, then the proof above applies to all components individually. Then the total number of bricks is smaller than or equal than the sum of all components, which is of course again within $\mathcal{O}(B^{\frac{2}{3}})$.

REFERENCES

- [1] K. Bentley, C. A. Franco, A. Philippides, R. Blanco, M. Dierkes, V. Gebala, F. Stanchi, M. Jones, I. M. Aspalter, G. Cagna *et al.*, “The role of differential VE-cadherin dynamics in cell rearrangement during angiogenesis,” *Nature Cell Biology*, vol. 16, no. 4, p. 309, 2014.
- [2] P. Blinder, P. S. Tsai, J. P. Kaufhold, P. M. Knutsen, H. Suhl, and D. Kleinfeld, “The cortical angiome: an interconnected vascular network with noncolumnar patterns of blood flow,” *Nature Neuroscience*, vol. 16, no. 7, p. 889, 2013.
- [3] R. Hägerling, C. Pollmann, M. Andreas, C. Schmidt, H. Nurmi, R. H. Adams, K. Alitalo, V. Andresen, S. Schulte-Merker, and F. Kiefer, “A novel multistep mechanism for initial lymphangiogenesis in mouse embryos based on ultramicroscopy,” *The EMBO Journal*, vol. 32, no. 5, pp. 629–644, 2013.
- [4] N. Hamilton, “Quantification and its applications in fluorescent microscopy imaging,” *Traffic*, vol. 10, no. 8, pp. 951–961, 2009.
- [5] D. Drees, A. Scherzinger, R. Hägerling, F. Kiefer, and X. Jiang, “Scalable robust graph and feature extraction for arbitrary vessel networks in large volumetric datasets,” *BMC Bioinform.*, vol. 22, no. 1, p. 346, 2021.
- [6] C. Kirst, S. Skriabine, A. Vieites-Prado, and N. Renier, “Mapping the fine-scale organization and plasticity of the brain vasculature,” *Cell*, vol. 180, pp. 780–795, 2020.
- [7] S. Zhao, M. Todorov, R. Cai, and A. Ertürk, “Cellular and molecular probing of intact human organs,” *Cell*, vol. 180, pp. 796–812, 2020.
- [8] L. Grady, “Random walks for image segmentation,” *IEEE Trans. Pattern Anal. Mach. Intell.*, vol. 28, no. 11, pp. 1768–1783, 2006.
- [9] Z. Wang, L. Guo, S. Wang, L. Chen, and H. Wang, “Review of random walk in image processing,” *Archives of Computational Methods in Engineering*, vol. 26, pp. 17–34, 2019.
- [10] Z. Shi, J. Ma, M. Zhao, Y. Liu, Y. Feng, M. Zhang, L. He, and K. Suzuki, “Many is better than one: an integration of multiple simple strategies for accurate lung segmentation in CT images,” *BioMed Research International*, vol. 2016, 2016.
- [11] R. Hägerling, D. Drees, A. Scherzinger, C. Dierkes, S. Martin-Almedina, S. Butz, K. Gordon, M. Schäfers, K. Hinrichs, P. Ostergaard, D. Vestweber, T. Goerge, S. Mansour, X. Jiang, P. S. Mortimer, and F. Kiefer, “VIPAR, a quantitative approach to 3D histopathology applied to lymphatic malformations,” *JCI Insight*, vol. 2, no. 16, 2017.
- [12] S. Mathewlynn and S. Collins, “Volume and vascularity: Using ultrasound to unlock the secrets of the first trimester placenta,” *Placenta*, vol. 84, pp. 32–36, 2019.
- [13] M. Vaithyanathan, N. Safa, and A. T. Melvin, “Fluorocelltrack: An algorithm for automated analysis of high-throughput droplet microfluidic data,” *PLoS ONE*, vol. 14, no. 5, p. e0215337, 2019.
- [14] Y. Chen, P. Huang, K. Lin, H. Lin, L. Wang, C. Cheng, T. Chen, Y. Chan, and J. Y. Chiang, “Semi-automatic segmentation and classification of pap smear cells,” *IEEE J. Biomed. Health Informatics*, vol. 18, no. 1, pp. 94–108, 2014.
- [15] T. Xie, Z. Wang, Q. Zhao, Q. Bai, X. Zhou, Y. Gu, W. Peng, and H. Wang, “Machine learning-based analysis of MR multiparametric radiomics for the subtype classification of breast cancer,” *Frontiers in Oncology*, vol. 9, p. 505, 2019.
- [16] T. Xie, Q. Zhao, C. Fu, Q. Bai, X. Zhou, L. Li, R. Grimm, L. Liu, Y. Gu, and W. Peng, “Differentiation of triple-negative breast cancer from other subtypes through whole-tumor histogram analysis on multiparametric MR imaging,” *European Radiology*, vol. 29, no. 5, pp. 2535–2544, 2019.
- [17] Z. Xu, U. Bagci, B. Foster, A. Mansoor, and D. J. Mollura, “Spatially constrained random walk approach for accurate estimation of airway wall surfaces,” in *Proc. of Medical Image Computing and Computer-Assisted Intervention (MICCAI), Part II*, ser. LNCS, K. Mori, I. Sakuma, Y. Sato, C. Barillot, and N. Navab, Eds., vol. 8150. Springer, 2013, pp. 559–566.
- [18] U. Bagci, J. K. Udupa, J. Yao, and D. J. Mollura, “Co-segmentation of functional and anatomical images,” in *Proc. of Medical Image Computing and Computer-Assisted Intervention (MICCAI), Part III*, ser. LNCS, N. Ayache, H. Delingette, P. Golland, and K. Mori, Eds., vol. 7512. Springer, 2012, pp. 459–467.
- [19] U. Bagci, J. K. Udupa, N. Mendhiratta, B. Foster, Z. Xu, J. Yao, X. Chen, and D. J. Mollura, “Joint segmentation of anatomical and functional images: Applications in quantification of lesions from PET, PET-CT, MRI-PET, and MRI-PET-CT images,” *Medical Image Anal.*, vol. 17, no. 8, pp. 929–945, 2013.
- [20] C. Gerlein-Safdi and C. S. Ruf, “A CYGNSS-based algorithm for the detection of inland waterbodies,” *Geophysical Research Letters*, vol. 46, no. 21, pp. 12 065–12 072, 2019.
- [21] J. Shen, Y. Du, W. Wang, and X. Li, “Lazy random walks for superpixel segmentation,” *IEEE Trans. Image Process.*, vol. 23, no. 4, pp. 1451–1462, 2014.
- [22] H. Wang, J. Shen, J. Yin, X. Dong, H. Sun, and L. Shao, “Adaptive nonlocal random walks for image superpixel segmentation,” *IEEE Trans. Circuits Syst. Video Technol.*, vol. 30, no. 3, pp. 822–834, 2020.
- [23] J. Li, S. Yang, X. Huang, Q. Da, X. Yang, Z. Hu, Q. Duan, C. Wang, and H. Li, “Signet ring cell detection with a semi-supervised learning framework,” in *Proc. of Information Processing in Medical Imaging - 26th International Conference (IPMI)*, ser. LNCS, A. C. S. Chung, J. C. Gee, P. A. Yushkevich, and S. Bao, Eds., vol. 11492. Springer, 2019, pp. 842–854.
- [24] S. Andrews, G. Hamarneh, and A. Saad, “Fast random walker with priors using precomputation for interactive medical image segmentation,” in *Proc. of Medical Image Computing and Computer-Assisted Intervention (MICCAI), Part III*, ser. LNCS, T. Jiang, N. Navab, J. P. W. Pluim, and M. A. Viergever, Eds., vol. 6363. Springer, 2010, pp. 9–16.
- [25] W. Yang, J. Cai, J. Zheng, and J. Luo, “User-friendly interactive image segmentation through unified combinatorial user inputs,” *IEEE Trans. Image Process.*, vol. 19, no. 9, pp. 2470–2479, 2010.
- [26] A. Bian and X. Jiang, “Statistical modeling based adaptive parameter setting for random walk segmentation,” in *Advanced Concepts for Intelligent Vision Systems*, J. Blanc-Talon, C. Distant, W. Philips, D. Popescu, and P. Scheunders, Eds. Springer, 2016, pp. 698–710.
- [27] L. Cerrone, A. Zeilmann, and F. A. Hamprecht, “End-to-end learned random walker for seeded image segmentation,” in *IEEE Conference on Computer Vision and Pattern Recognition (CVPR)*, 2019, pp. 12 559–12 568.
- [28] M. Li, H. Gao, F. Zuo, and H. Li, “A continuous random walk model with explicit coherence regularization for image segmentation,” *IEEE Trans. Image Process.*, vol. 28, no. 4, pp. 1759–1772, 2019.
- [29] J. Prassni, T. Ropinski, and K. Hinrichs, “Uncertainty-aware guided volume segmentation,” *IEEE Transactions on Visualization and Computer Graphics*, vol. 16, no. 6, pp. 1358–1365, 2010.
- [30] Y. Xiao and J. Hu, “Hierarchical random walker for multimodal brain tumor segmentation,” *MICCAI Challenge on Multimodal Brain Tumor Segmentation*, 2012.
- [31] L. Ge, R. Ju, T. Ren, and G. Wu, “Interactive RGB-D image segmentation using hierarchical graph cut and geodesic distance,” in *Pacific Rim Conference on Multimedia*. Springer, 2015, pp. 114–124.

- [32] Y. Boykov and M. Jolly, "Interactive graph cuts for optimal boundary and region segmentation of objects in N-D images," in *Proc. of the Eighth International Conference on Computer Vision (ICCV), Volume 1*. IEEE Computer Society, 2001, pp. 105–112.
- [33] A. Fabijanska and J. Goclawski, "The segmentation of 3d images using the random walking technique on a randomly created image adjacency graph," *IEEE Trans. Image Process.*, vol. 24, no. 2, pp. 524–537, 2015.
- [34] P. D. Lösel, T. van de Kamp, A. Jayme, A. Ershov, T. Faragó, O. Pichler, N. T. Jerome, N. Aadepe, S. Bremer, S. A. Chilingaryan, M. Heethoff, A. Kopmann, J. Odar, S. Schmelzle, M. Zuber, J. Witzbrodt, T. Baumbach, and V. Heuveline, "Introducing biomedisa as an open-source onlineplatform for biomedical image segmentation," *Nature Communications*, vol. 11, p. 5577, 2020.
- [35] C. Hu, H. Hui, S. Wang, D. Dong, X. Liu, X. Yang, and J. Tian, "Cerebral vessels segmentation for light-sheet microscopy image using convolutional neural networks," in *Medical Imaging: Biomedical Applications in Molecular, Structural, and Functional Imaging*, 2017, p. 101370K.
- [36] G. Litjens, T. Kooi, B. E. Bejnordi, A. A. A. Setio, F. Ciompi, M. Ghafoorian, J. A. W. M. van der Laak, B. van Ginneken, and C. I. Sánchez, "A survey on deep learning in medical image analysis," *Medical Image Anal.*, vol. 42, pp. 60–88, 2017.
- [37] Z. Wang, L. Guo, S. Wang, L. Chen, and H. Wang, "Review of random walk in image processing," *Archives of Computational Methods in Engineering*, vol. 26, no. 1, pp. 17–34, 2019.
- [38] Q. Li, L. Chen, X. Li, X. Lv, S. Xia, and Y. Kang, "PRF-RW: a progressive random forest-based random walk approach for interactive semi-automated pulmonary lobes segmentation," *Int. J. Mach. Learn. Cybern.*, vol. 11, no. 10, pp. 2221–2235, 2020.
- [39] E. LaMar, M. A. Duchaineau, B. Hamann, and K. I. Joy, "Multiresolution techniques for interactive texture-based rendering of arbitrarily oriented cutting planes," in *Proc. of Joint Eurographics and IEEE TCVG Symposium on Visualization, VisSym*, W. C. de Leeuw and R. van Liere, Eds. Eurographics Association, 2000, pp. 105–114.
- [40] M. Weiler, R. Westermann, C. D. Hansen, K. Zimmerman, and T. Ertl, "Level-of-detail volume rendering via 3D textures," in *Proc. of Visualization and Graphics Symposium, (VVS)*, W. E. Lorensen, R. Crawfis, and D. Cohen-Or, Eds. ACM / IEEE Computer Society, 2000, pp. 7–13.
- [41] T. Brix, J.-S. Praßni, and K. Hinrichs, "Visualization of large volumetric multi-channel microscopy data streams on standard PCs," in *BioVis: 4th Symposium on Biological Data Visualization*, 2014.
- [42] C. Crassin, F. Neyret, S. Lefebvre, and E. Eisemann, "Gigavoxels: ray-guided streaming for efficient and detailed voxel rendering," in *Proc. of Symposium on Interactive 3D Graphics (SI3D)*, E. Haines, M. McGuire, D. G. Aliaga, M. M. Oliveira, and S. N. Spencer, Eds. ACM, 2009, pp. 15–22.
- [43] F. Wang, I. Wald, and C. R. Johnson, "Interactive rendering of large-scale volumes on multi-core cpus," in *9th IEEE Symposium on Large Data Analysis and Visualization (LDAV)*. IEEE, 2019, pp. 27–36.
- [44] W. Hackbusch, *Iterative Solution of Large Sparse Systems of Equations*, ser. Applied Mathematical Sciences. Springer, 1994, vol. 95.
- [45] D. Drees and X. Jiang, "Bayesian reasoning based adaptive parameter setting for random walk segmentation under arbitrary noise models," *in preparation*.
- [46] S. D. Olabbarriaga and A. W. M. Smeulders, "Interaction in the segmentation of medical images: A survey," *Medical Image Anal.*, vol. 5, no. 2, pp. 127–142, 2001.
- [47] H. Gueziri, M. J. McGuffin, and C. Laporte, "Latency management in scribble-based interactive segmentation of medical images," *IEEE Trans. Biomed. Eng.*, vol. 65, no. 5, pp. 1140–1150, 2018.
- [48] B. Rister, D. Yi, K. Shivakumar, T. Nobashi, and D. L. Rubin, "CT-ORG, a new dataset for multiple organ segmentation in computed tomography," *Sci Data*, vol. 7, no. 1, pp. 1–9, 2020.
- [49] N. Kirschnick, D. Drees, E. Redder, R. Erapaneedi, A. P. da Graca, M. Schäfers, X. Jiang, and F. Kiefer, "Rapid methods for the evaluation of fluorescent reporters in tissue clearing and the segmentation of large vascular structures," *Science*, vol. 24, no. 6, p. 102650, 2021.
- [50] G. Hamarneh and P. Jassi, "Vascusynth: Simulating vascular trees for generating volumetric image data with ground truth segmentation and tree analysis," *Computerized Med. Imaging and Graphics*, vol. 34, no. 8, pp. 605–616, 2010.
- [51] D. Drees and X. Jiang, "Efficiently sampling large images from bounded functions," *in preparation*.
- [52] H. F. Inman and E. L. Bradley Jr, "The overlapping coefficient as a measure of agreement between probability distributions and point

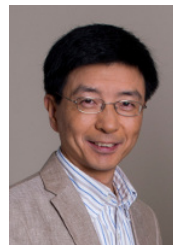
- estimation of the overlap of two normal densities," *Communications in Statistics-Theory and Methods*, vol. 18, no. 10, pp. 3851–3874, 1989.
- [53] J. Meyer-Spradow, T. Ropinski, J. Mensmann, and K. H. Hinrichs, "Voreen: A rapid-prototyping environment for ray-casting-based volume visualizations," *IEEE Computer Graphics and Applications*, vol. 29, no. 6, pp. 6–13, 2009.



Dominik Drees received the M.S. degree in computer science from University of Münster, Germany, in 2016 and is currently pursuing the Ph.D. degree. His research interest are biomedical image processing and analysis with a focus on scalable out-of-core methods.



Florian Eilers received the M.S. degree in computational life science from University of Lübeck, Germany, in 2020 and is currently pursuing the Ph.D. degree. His research interest are biomedical image processing and analysis with a focus on complex valued images and complex valued neural networks.



Xiaoyi Jiang studied Computer Science at Peking University and received his Ph.D. and Venia Docendi (Habilitation) degree in Computer Science from University of Bern, Switzerland. He was an Associate Professor at Technical University of Berlin, Germany. Since 2002 he is a Full Professor at University of Münster, Germany. Currently, he is Editor-in-Chief of International Journal of Pattern Recognition and Artificial Intelligence. In addition, he also serves on the Advisory Board and Editorial Board of several journals, including International Journal of Neural Systems, and Journal of Big Data. He is a Senior Member of IEEE and Fellow of IAPR.